In operando mass transport imaging in microfluidic fuel cells

Marine Garcia, Alain Sommier, Jean Christophe Batsale, Stéphane Chevalier

In operando mass transport imaging in microfluidic fuel cells

M. GARCIA[a], A. SOMMIER[a], J.-C. BATSALE[a], S. CHEVALIER[a]

a. Arts et Metiers Institute of Technology, I2M UMR CNRS 5295, Bordeaux University, CNRS, Esplanade des Arts et Métiers, 33405 Talence Cédex, FRANCE, stephane.chevalier@u-bordeaux.fr

Abstract

Microfluidic fuel cells (MFC) are microfluidic electrochemical conversion devices which are used to power small electrical equipments. Their performance relies on the abilities to enhance the mass transfer between the reactants (fuel and oxidant) and the current generated. In this work, a novel in operando imaging technique to measure the concentration field of the reactants in a MFC is reported. This method is based on the visible spectroscopy which enables to link the light intensity passing through the MFC to its local reactant concentration. A MFC specifically developed for imaging studies was built and operated using acid formic and permanganate potassium as fuel and oxidant, respectively. The 2D transient concentration field of permanganate near the electrode were imaged and compared to a 3D numerical model of the MFC. An excellent agreement between them was found, and the mass transfer through the Damkhöler and Peclet number values was thoroughly assessed. This work paves the way toward advanced imaging techniques for in operando mass and charge transport characterizations of microfluidic electrochemical conversion devices.

Key words : Fuel cells, Imaging, Spectroscopy, Mass transfer, Microfluidic, Concentration fields, Mass diffusion, Semianalytical modelling.

1 Introduction

Microfluidic fuel cells (MFC) are particular microfluidic devices used to convert the chemical energy contained in fuels directly into electricity [1]. Such devices are composed of a microfluidic channel which ensures a rather good control of the hydrodynamic condition. Two electrodes are also embedded where the electrochemical reaction takes place: an oxidation at the anode and a reduction at the cathode. Such kind of MFC can be used both in galvanostatic or electrolysis mode which makes this technology a promising candidate for energy conversion and storage. There exists a wide variety of MFCs in the literature, and the reader is referred to the following comprehensive reviews for more details about them [2, 3, 4]. In the present work, the study is focused on a common membraneless MFC using acid formic (HCOOH) and potassium permanganate ($KMnO_4$) as this system is relatively robust, need few material, used non hazardous chemical, and is easy to operate.

Three main phenomena govern the MFC performances. One can cite first the mass transport based both on the diffusion and hydrodymanic of the species in the microchannel. The second transfer is linked to

the charge transfer in the electrolyte and the electrodes. Several authors reported a thorough description of such [5, 6]. And the last but not the least, the entropy generated during the energy conversion is transformed into heat which impact the rate of the mass diffusion and the electrochemical kinetic. Thus, the optimal performances of the MFC rely on a precise control and knowledge of these transfers. Such need is a claim for developing new in operando and contactless imaging method for MFC multiphysic characterisation.

Several studies in the literature have shown the great interest to use imaging method to characterize the mass transport [7, 8, 9, 10]. For example, Sun et al. [8] have used an optical microscope to study the permanganate diffusion into acid formic. Their work was mainly qualitative to illustrate the hydrodynamic flow in the MFC. Lu et al. [11] also used optical and fluorescence imaging techniques to validate their MFC model, and to measure the concentration distribution profile at one position in the channel. More advanced techniques based on infrared [12] or X-ray [13] can also be used to characterize the MFC structures or concentration or flow distribution. However, to date no thorough in operando characterization of the mass transport simultaneously with the current produced by a MFC was reported. Such study would be of prime interest for both MFC designers or/and advanced numerical models as it would enable the measurement of the main parameters governing the cell performances as the mass diffusivity, the electrochemical kinetics and reactant concentration distribution among others.

The main goal of the present work is to report the use of visible spectroscopy to measure the MFC mass transport during the cell operation. Such technique was already used for various concentration measurements in microfluidic [14] and this would be well adapted for MFC transient concentration field measurements. Thus, used in combination with a MFC model including the hydrodynamics, the mass, and the charge transport, it would enable to estimate MFC physical properties and performances. In the first section, a description of the MFC design specifically chosen for visible spectroscopy, and the associated imaging setup is described. It is followed by the MFC model. In the result section, the experimental concentration fields are presented and compared to the model. A thorough analysis of the technique is performed and its limitations are discussed.

2 Methods

2.1 Fabrication of the MFC

The T-shaped microfluidic channel was fabricated using standard photolithography. A negative photoresist was spin coated on a silicon wafer, covered with a photomask and exposed to UV light. It was then submerged in a propylene glycol methyl ether acetate (PGMEA) solution for the development. The obtained mold was placed in a Petri dish and coated with 5 mm of polydiméthylsiloxane (PDMS). After being cured, the PDMS was peeled off the mold and was hole-punched to create two inlets and one outlet. The microchannel height is 20 µm and the width is 3 mm. This specific aspect ratio was used to simplify the MFC model (see next section).

For the electrodes, an inverse pattern was first created on a glass wafer using the same photolithography process than for the PDMS stamp. The deposition was achieved through sputtering 60 nm of titanium as an adhesion layer and subsequently 300 nm of platinum for the catalyst material. The remaining

photoresist was removed by submerging the wafer in a chemical etching solution in order to obtain only the platinum pattern directly on the glass substrate. The PDMS stamp was plasma activated and bound to the glass substrate, resulting in the complete MFC presented Figure 1.

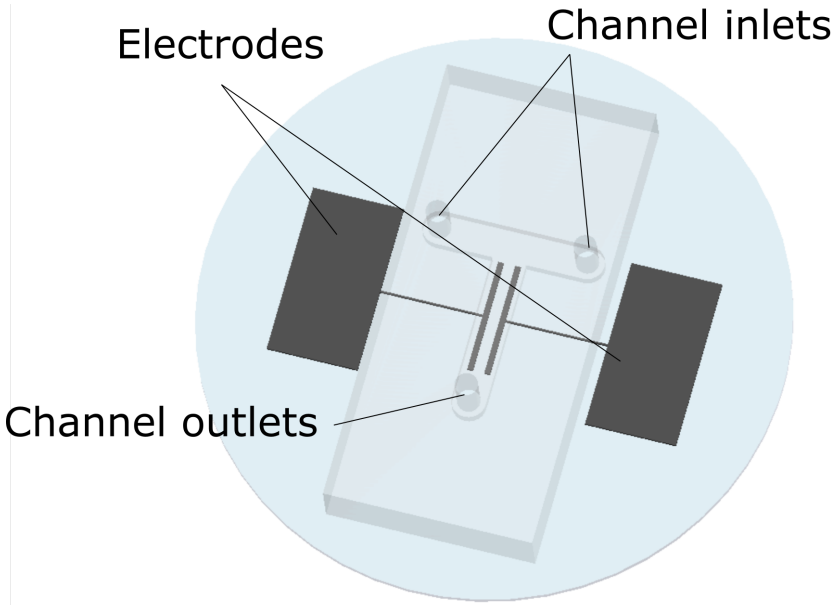

Figure 1: 3D view of the MFC.

2.2 Experimental setup

The measurements of the concentration distribution and the total current produced by the MCF were performed using the setup described in Figure 2. It is made of an home-made inverse microscope. A white colimated light is used as primary light source. A narrow band pass filter ($\lambda = 540 \pm 5$ nm) is used to produce a monochromatic green ligh passing through the MFC. The light is finally collected through a microscope objective and a lens to produce an image on a CMOS camera (Zelux 1.6 MP Color CMOS Camera). Only the green channel of the camera was used in the image post-processing.

The MFC is controlled using a potentiostat to measure the voltage and the current produced. An Ag/AgCl reference electrode was used to measure both anode and cathode potentials. The reactant flow rate are controlled using a syringe pump over a wide range from 0.5 to 100 µl/min.

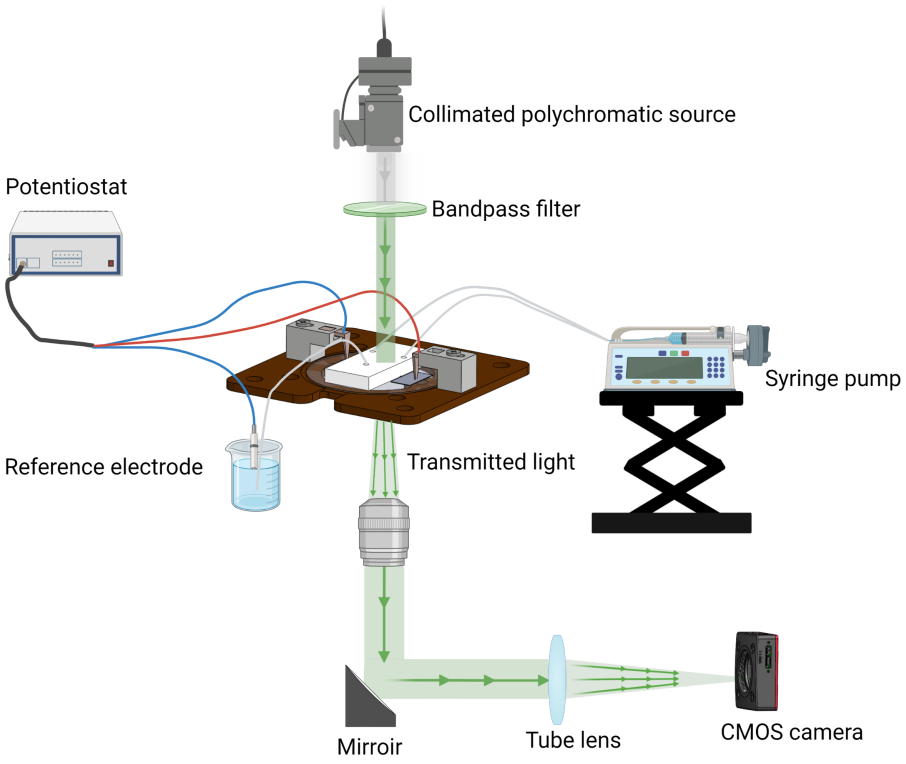

Figure 2: Schematic of the visible spectroscopic imaging setup used to measure the in operando concentration.

The reactants (acid formic and permanganate potassium) were especially chosen to have good MFC performances [1]. In addition, the permanganate potassium has a great advantage to have a clear absorption signature in the visible range whereas the formic acid is transparent. At the anode, the formic acid oxidation is:

$$HCOOH \longrightarrow CO_2 + 2H^+ + 2e^-, \tag{1}$$

and the cathode, the permanganate reduction is:

$$MnO_4^- + 8H^+ + 5e^- \longrightarrow Mn^{2+} + 4H_2O. \tag{2}$$

In equation 2, one can notice that when a current is produced, the permanganate ions (MnO_4^-) are transformed in manganese ions Mn^{2+}. Thus, when a current is applied through the MFC electrode, it triggers a decrease of the permanganate concentration, and it is this concentration variation which can be measured by visible spectroscopy.

The wavelength chosen in the imaging setup correspond to the strongest light absorption of the permangante ions whereas the formic acid is completely transparent. Thus, using the Beer-Lambert one can link the variation of light intensity to the variation of permengante concentation as

$$\Delta c = -\kappa h \log_{10}\left(\frac{I_0 + \Delta I}{I_0}\right), \tag{3}$$

where κ is the permanganate absorptivity (mM/µm), h the channel height (µm), and I_0 is the light

intensity of the background and ΔI the light intensity variation induced by the current production. The permanganate absorptivity coefficient was measured to be $\kappa = 7.27$ mM/µm at 540 nm.

2.3 3D mass transfer model

2.3.1 General equations

The 3D channel with one single electrode is presented in Figure 3. In order to simplify the model with only the most important phenomena, the following assumption have been made :

- the velocity profile is considered laminar and established ;
- the mass diffusivity is considered constant ;
- the problem is solved in steady state ;
- the Fick law is used to modelled the mass diffusion in diluted solution ;
- the ions and the reactants in the electrolyte and in the anolyte do not interact on the mass and charge transport at the cathode ;
- the electrochemical reaction is modelled by a Tafel law ;

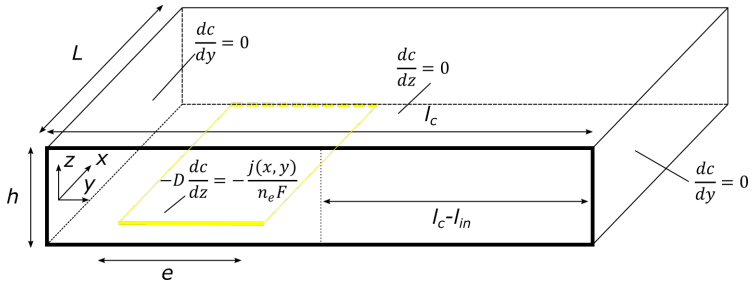

Figure 3: 3D schematic of the channel with a single electrode placed at $z = 0$ (in yellow). The boundary conditions are also indicated.

In these conditions, the 3D problem of the mass transport can be written as :

$$v(y,z)\left(\frac{\partial c}{\partial x}+\frac{\partial c}{\partial y}+\frac{\partial c}{\partial z}\right) = D\left(\frac{\partial^2 c}{\partial x^2}+\frac{\partial^2 c}{\partial z^2}+\frac{\partial^2 c}{\partial y^2}\right), \tag{4}$$

$$\left.\frac{\partial c}{\partial y}\right|_{y=0,l_c} = 0, \tag{5}$$

$$\left.\frac{\partial c}{\partial y}\right|_{x=L} = 0, \tag{6}$$

$$-D\left.\frac{\partial c}{\partial z}\right|_{z=0} = -\frac{j(x,y)}{n_e F}, \tag{7}$$

$$\left.\frac{\partial c}{\partial z}\right|_{z=h} = 0, \tag{8}$$

$$c(x=0,y,z) = c_0(y), \tag{9}$$

where c is the reactant concentration (M), D is the mass diffusivity (m^2/s), x, y, z are the spacial coordinates (m), n_e is the number of electron exchanged, F is the Faraday constant (C/mol) and $j(x, y)$ is the current density distribution (A/m^2) on the electrode. It is zero outside it. The current density is modelled using the Tafel law which links the local reactant concentration to the fuel cell potential as :

$$j(x, y) = i_0 \frac{c(x, y, z = 0)}{c_0} \exp(\eta/b), \tag{10}$$

where i_0 is the electrode exchange current (A/m^2), b the Tabel slope (V) and η the overpotential (V) linked to the electrode potential. The velocity profile, $v(x, y, z)$ can be written analytically under the assuption of a Poiseuille velocity profile in a rectangular channel as [6, 15]

$$v_x(y, z) = \frac{4h^2 \Delta p}{\pi^3 \mu L} \sum_{n,odd}^{\infty} \frac{1}{n^3} \left[1 - \frac{\cosh(n\pi \frac{2y - l_c}{2h})}{\cosh(n\pi \frac{l_c}{2h})} \right] \sin\left(n\pi \frac{z}{h} \right), \tag{11}$$

where h, L and l_c are the channel dimensions indicated in Figure 3, p is the pressure (Pa) and μ is the viscosity (Pa.s).

2.3.2 Model simplification and solution

Given the geometry and the operating conditions of the MFC described in the previous section, one can simplified the previous general model in two dimensions using the following assumptions :

- the Peclet number in the x-direction is considered large enough to neglected the diffusion in this direction, i.e. $Pe \gg 1$ and $\partial^2 c/\partial x^2 \approx 0$;
- the Poiseuille flow implies that the flow velocity in the y- and z-direction can be neglected ;
- the aspect ratio of the channel is considered large enough to neglect the diffusion in the z-direction compared to the others, i.e. $\gamma = l_c/h \gg 1$ and $\partial^2 c/\partial z^2 \approx j(x, y)/(n_e F D h)$.

In addition, the previous model can be rewritten using the dimentionless variables $\tilde{c} = c/c_0$, $\tilde{y} = y/l_c$, $\tilde{x} = x/x_e$ with $x_e = \bar{v} l_c^2/D$ is the x scale length [5], and $\bar{v} = q_{tot}/(h l_c)$ is the reactants average velocity. This leads to:

$$f(\tilde{y}) \frac{\partial \tilde{c}}{\partial \tilde{x}} = \frac{\partial^2 \tilde{c}}{\partial \tilde{y}^2} - K(\tilde{x}, \tilde{y}) \tilde{c}, \tag{12}$$

$$\left. \frac{\partial \tilde{c}}{\partial \tilde{y}} \right|_{\tilde{y}=1} = 0, \tag{13}$$

$$\left. \frac{\partial \tilde{c}}{\partial \tilde{y}} \right|_{\tilde{y}=0} = 0, \tag{14}$$

$$\tilde{c}(x = 0, \tilde{y}) = \Theta(\tilde{y} - (l_c - l_{in})/l_c), \tag{15}$$

where $f(\tilde{y})$ is obtained from the integration of the velocity profile (11) in the x-direction as:

$$f(\tilde{y}) = \frac{1}{1-0,63/\gamma}\left(1-\sum_{n,odd}^{\infty}\frac{96}{(n\pi)^4}\frac{\cosh(n\pi\gamma(2\tilde{y}-1)}{\cosh(n\pi\frac{\gamma}{2})}\right), \tag{16}$$

Θ is the Heaviside function modelling the initial reactant concentration distribution, and K is a dimensionless Damkhöler [6] number defined as

$$K = \begin{cases} Da & \text{if} \quad \tilde{x},\tilde{y} \in \Omega_e \\ 0 & \text{else} \end{cases} \tag{17}$$

where Ω_e is the electrode domain and $Da = kl_c^2/(hD)$ where $k = i_c^0/(n_e F c_0)e^{\eta/b}$ is the electrochemical kinetics coefficient (m/s).

The previous system has no evident analytical solution. It is solved using a numerical scheme based on Finite Differences to approximate the Laplacian the $\tilde{y}$-direction and a Runge-Kutta algorithm in the $\tilde{x}$-direction. Such numerical model is written using Matlab and the sub routine *ode15s* was used for the Runge-Kutta integration scheme. A number a 150 elements in the $\tilde{y}$-direction were used in the Finite Difference mesh, and this was considered enough to ensure the mesh independence.

Once the concentration field is solved, the current density produced by the cell can be estimated as

$$I_{tot} = n_e F q_c c_0 \varepsilon, \tag{18}$$

where q_c is the permanganate solution flow rate, and ε is the cell efficiency defined as:

$$\varepsilon = 1 - \frac{\int_0^1 \tilde{c}(\tilde{y},\tilde{x}=L_e/x_e)d\tilde{y}}{\int_0^1 \tilde{c}(\tilde{y},\tilde{x}=0)d\tilde{y}}. \tag{19}$$

3 Results

3.1 Image acquisition

The images were acquired using the setup described in Figure 2. The camera frame rate was set to 10 fps. The cell was imaged first at rest during few seconds before to start producing a current. The anode and cathode flow rate were set 1 and 0.5 µl/min, respectively, for five minute before to start the experiment to ensure that the flow is fully developed. Such flow rate ensure an average velocity of 0.42 mm/s and a residence time of 24 s.

In Figure 4(a), a complete image of the MFC is presented where the channel (in green) and the electrodes (in black) are visible. Only the concentration field around the electrodes can be recorded since they are opaque to the visible light. At $t = 0$ s, a current of 20 µA is generated by the MFC for 30 s and the images were kept recording during 1 min. Such protocol ensures the measurement of the transient response of the concentration field before to reach the steady state, and the measurement of the permanganate concentration relaxation after that the current was switched off. A typical 10 bits greyscale image recorded is presented in Figure 4(b). It is located at the cathode where the permanganate is consumed as predicted

in equation 2. The transient profile of the current and of the light intensity is also presented in Figure 4(c).

In the results presented in Figure4(c), it is observed that the current triggers a change in light intensity of about 10 - 15 counts, i.e. less than 1.5%. Then, when the current is switched off, the light intensity slowly decreases back to its initial value. Such behaviour is explained as follow. When the permanganate is consumed, the light is less absorbed by the solution and the medium becomes more transparent. When the current is off, the continuous flow rate slowly brings back the permanganate concentration at its initial state. It can be note that the approximative 25 s that the light intensity took to be back to its initial value correspond roughly to the residence time of the solution in the MFC. Thus, the results in Figure4 were expected and confirmed the right development of the setup and the right operation of the MFC.

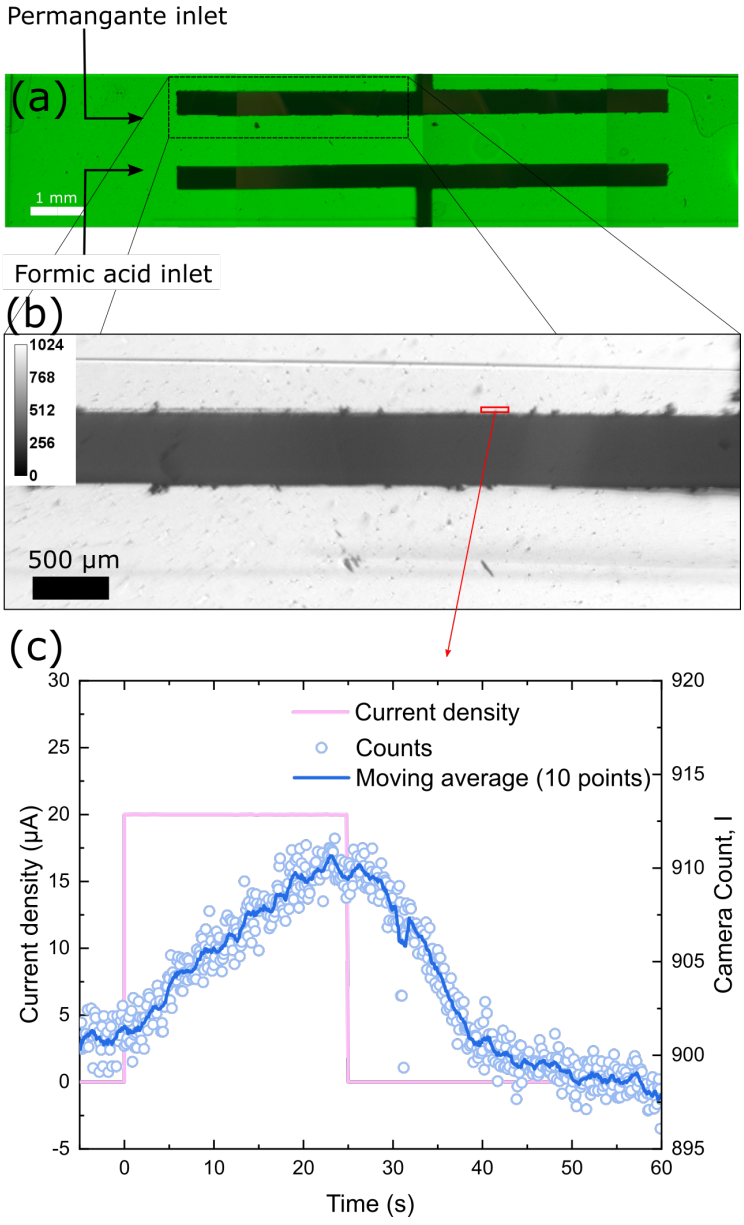

Figure 4: (a) Full image of the MFC in green light. (b) A typical 10 bits images recorded. The red rectangle indicates the area used to extract the temporal data. (c) Temporal evolution of the current density and the camera counts variation recorded during the experiments. A moving average is added to guide the eyes.

3.2 Concentration maps and profile

The greyscale images are converted to concentration fields using the Beer-Lambert law described in equation 3. The background image is taken as the average of all the images recorded before than the current was switched on. Then the Beer-Lamber law is applied on each pixel on each image to obtain a stack of concentration field. Once the concentration variation was measured using this technique, the absolute concentration field is computed as $c(x, y, t) = c_0 - \Delta c(x, y, t)$.

In Figure 5(a) to (e), the concentration field are presented for a range of time. As expected, before than the current was triggered, the concentration field is uniform. Then, a gradient of concentration appears and diffuses (see Figure 5(b) to (d)). It is more pronounced toward the end of the channel than at the inlet due to the effect of the convection. A maximum decrease of 2 mM is observed which is a rather small quantity of concentration variation which was able to measured. From the data presented in Figure 5, a noise of ± 0.2 mM is estimated. Such results highlights the somewhat quite good sensitivity of the setup to detect rather small concentration variations in MFC.

In Figure 5(f), several transient concentration profiles are presented for a range of vertical positions in the channel: from the border of the electrode (0 µm) to 200 µm far from it. As expected, as soon as the current is triggered (at $t = 0$ s), the concentration starts to decrease first at the electrode interface before to slowly diffuse toward the channel. At 150 µm, the concentration profile start to decrease 13 s after the current was triggered. And after 200 µm, no more concentration variation is visible in this region of the MFC. Such concentration length is governed by the Peclet number [16].

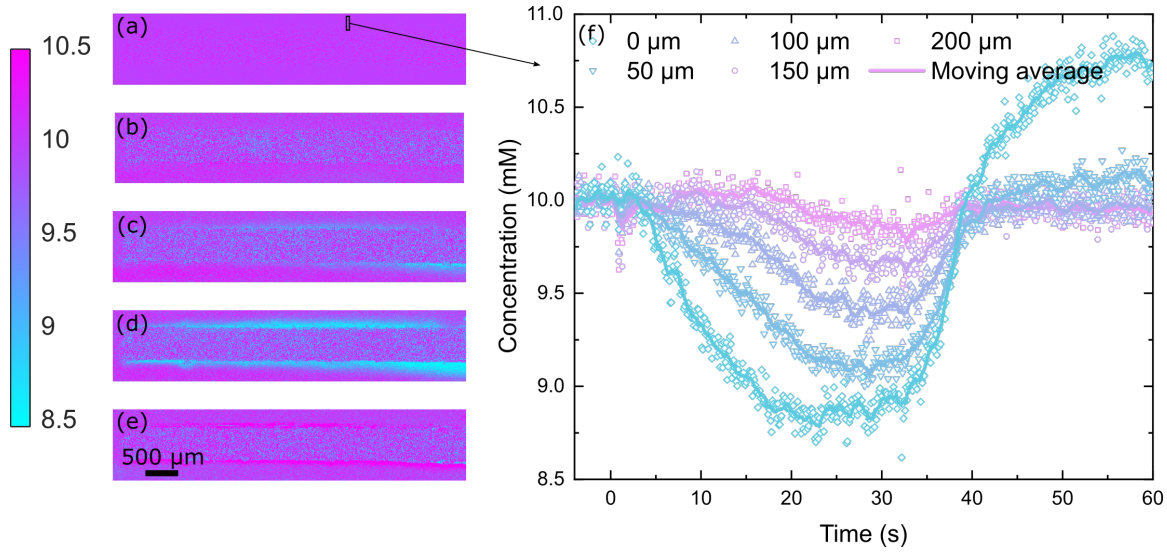

Figure 5: From (a) to (e), concentration maps obtained by visible spectroscopy for several times (before the current gate, at 10 s, 20 s and 30 s after, and at 60 s when the current is off). (f) Temporal evolution of the concentration variation close to the electrode for several positions. The mobile averages were added as eye guide. The black rectangle in (a) indicates the x-position where the temporal concentration profiles were taken.

In Figure 5(e) and (f) for the profile close to the electrode, an increase of concentration is observed. Such behavior is due to the formation of manganese oxide (see equation 2) which is non soluble and get trapped at the bottom of the channel. Such side product of the reaction was already observed in some previous studies [4]. It is known to decrease the MFC performance and to degrade the electrode material. However, in our case, the MFC can be cleaned up using some isopropanol after the experiment. Thus, the proposed imaging setup is a powerful tool to study this side reaction and to help developing future efficient strategy to get rid of it in order to improve the MFC performances and life-time.

3.3 Comparison with the model in steady states

In the last section of this work, the numerical model and the experimental data are compared to validate the study. In the numerical model, all the operating conditions are set identicals (flow rates, current density, MFC dimensions) to the experiments. The only unknown parameter remain the effective diffusivity of the permanganate in aqueous solution. This parameter was measured to be $D = 2 \times 10^{-3}$ mm^2/s in a forthcoming study. The corresping Peclet number is obtained to be 625. The other parameter: the kinetic coefficient k, was obtained using an iterative algorithm to satisfy a total current of 20 µA. It is found to be 1.54×10^{-3} mm/s, leading to a Damkhöler number of 348 and a fuel cell efficiency of almost 50%. The resulting concentration field is presented in Figure 6(a). A black rectangle was added at the electrode position.

In order to match the steady state assumption of the model, the experimental concentration field just before the current was switched off was used (i.e. at $t = 25$ s) and average over 2 s. At this time, it was noticed that the steady state was reached. This concentration field is presented in Figure 6(b), and qualitatively, the same order of concentration variation can be observed in both the numerical and experimental data. It is important to note, that no parameter were fitted to achieve such results in the model.

Moving forward, the concentration profiles at three channel positions were extracted to be compared. They are indicated in Figure 6(a): one at the inlet, one at the middle and the last one toward the end. These profiles are presented in Figure 6(c) and an excellent agreement with the model is found. The concentration gradient increase with the channel position as expected. Some small deviations are however observed toward the end of the channel (position 3) which may due to some flow instability observed during the experiment or the presence of manganese oxide previously noticed. This ultimate result validates both the experimental setup and the MFC developed and the assumption made in the numerical simulation to model the mass and charge transfer in MFCs.

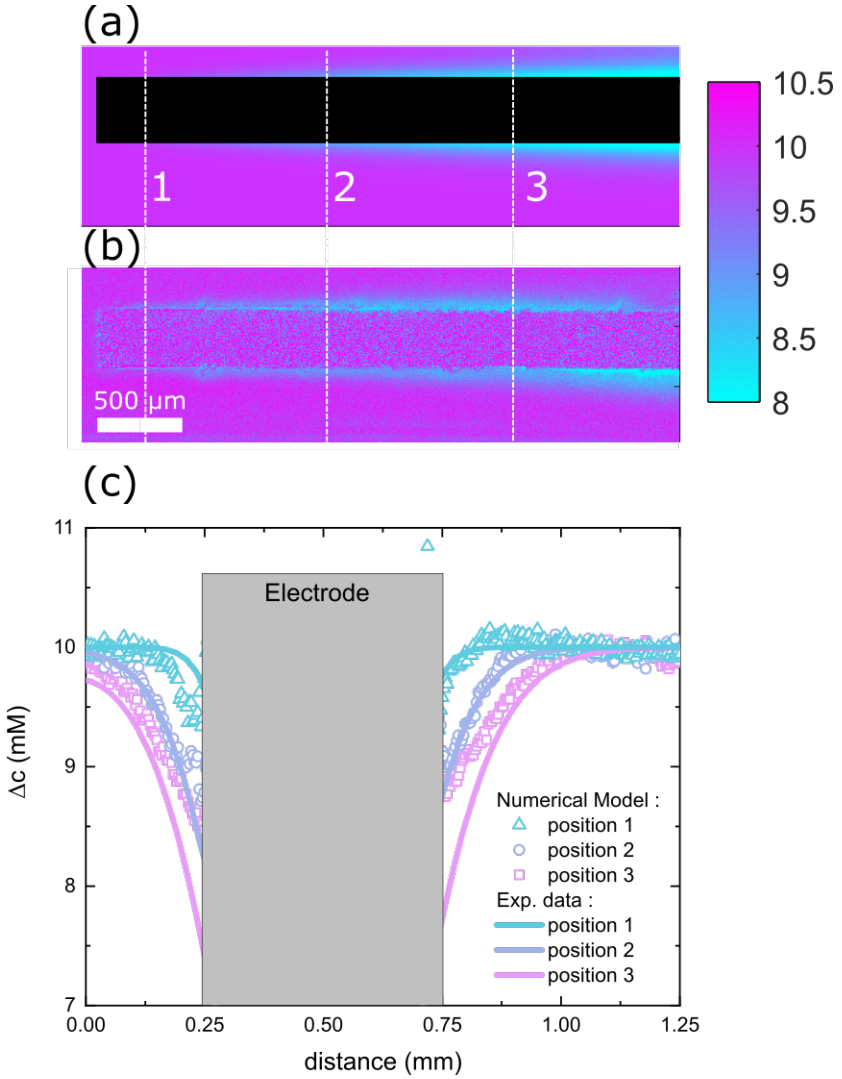

Figure 6: (a) Numerical simulation of the concentration field for a current of 20 µA. (b) Concentration field measured by visible spectroscopy at the same current 25 s after the current was triggered . The color bar indicates the concentration in mM. (c) Comparison of the numerical and experimental concentration distribution for several positions in the channel. The 0 corresponds to the MFC top wall.

4 Conclusion

In this work, an in operando MFC was imaged using visible spectroscopy. A specific imaging setup and MFC were developed to achieve this target. The concentration fields were measured based on the Beer-Lambert law enabled to measure reactant concentration variations as low as 0.2 mM when a current is triggered. The obtained image were the first reported in the literature, and opens the gate to advance imaging technique for MFC characterizations.

Along with the experimental data, a numerical simulation of the 3D problem taking into account the velocity field, the mass diffusion and the electrochemical reaction at the electrode was developed. All the parameter of this model were known or measure ex situ. By comparing the simulation to the experimental data, an excellent agreement was found. In particular, the Peclet number and the Damkhöler number were found to be 625 and 348, respectively, indicating that the electrochemical kinetic are quite

fast and that the diffusion is the limiting factor. Such limiting diffusion configuration is expected to obtain a large MFC efficiency , i.e. 50% in the present work.

Finally, this work demonstrates the feasibility to both image and model the transient concentration fields in a MFC. These data were used to thoroughly analyse the mass transfer which are a prime importance to improve the MFC performance and efficiency. With these techniques one can improve the operating conditions and the MFC design for more powerful electrochemical energy conversion systems.

Acknowledgement

The author gratefully acknowledges the French National Research Agency (ANR) for its support through the project I2MPAC, Grant No. ANR-20-CE05-0018-01. Mr Gérald Clisson and D. Michaud are warmly thanked for their technical assistance during the fabrication of the MFC.

References

[1] Erik Kjeang, Ned Djilali, and David Sinton. Microfluidic fuel cells: A review. *Journal of Power Sources*, 186(2):353–369, jan 2009.

[2] Omar A. Ibrahim, Marina Navarro-Segarra, Pardis Sadeghi, Neus Sabaté, Juan Pablo Esquivel, and Erik Kjeang. Microfluidics for Electrochemical Energy Conversion. *Chemical Reviews*, page acs.chemrev.1c00499, jan 2022.

[3] Yuan Zhou, Xun Zhu, Yang Yang, Dingding Ye, Rong Chen, and Qiang Liao. Route towards high-performance microfluidic fuel cells: a review. *Sustainable Energy and Fuels*, 5(11):2840–2859, 2021.

[4] Yifei Wang, Shijing Luo, Holly Y.H. Kwok, Wending Pan, Yingguang Zhang, Xiaolong Zhao, and Dennis Y.C. Leung. Microfluidic fuel cells with different types of fuels: A prospective review. *Renewable and Sustainable Energy Reviews*, 141(January):110806, may 2021.

[5] Martin Z. Bazant, Katsuyo Thornton, and Armand Ajdari. Diffuse-charge dynamics in electrochemical systems. *Physical Review E*, 70(2):021506, aug 2004.

[6] Stéphane Chevalier. Semianalytical modeling of the mass transfer in microfluidic electrochemical chips. *Physical Review E*, 104(3):035110, sep 2021.

[7] Seung-Wu Lee and Yoomin Ahn. Influence of electrode groove geometry on the passive control of the depletion layer in microfluidic fuel cells. *Journal of Micromechanics and Microengineering*, 25(12):127001, dec 2015.

[8] M.H. Sun, G. Velve Casquillas, S.S. Guo, J. Shi, H. Ji, Q. Ouyang, and Y. Chen. Characterization of microfluidic fuel cell based on multiple laminar flow. *Microelectronic Engineering*, 84(5-8):1182–1185, may 2007.

[9] Amandeep Jindal, Suddhasatwa Basu, Neha Chauhan, Tomofumi Ukai, D. Sakthi Kumar, and K.T. Samudhyatha. Application of electrospun CNx nanofibers as cathode in microfluidic fuel cell. *Journal of Power Sources*, 342:165–174, feb 2017.

[10] Chunmei Liu. Potassium Permanganate as an Oxidant for a Microfluidic Direct Formate Fuel Cell. *International Journal of Electrochemical Science*, 14(5):4557–4570, apr 2019.

[11] Xu Lu, Yifei Wang, Dennis Y.C. Leung, Jin Xuan, and Huizhi Wang. A counter-flow-based dual-electrolyte protocol for multiple electrochemical applications. *Applied Energy*, 217(February):241–248, may 2018.

[12] S. Chevalier, J.-N. Tourvieille, A. Sommier, and C. Pradère. Infrared thermospectroscopic imaging of heat and mass transfers in laminar microfluidic reactive flows. *Chemical Engineering Journal Advances*, 8:100166, nov 2021.

[13] Konosuke Watanabe, Takuto Araki, Takuya Tsujiguchi, and Gen Inoue. Influence of the Diffusion Media Structure for the Bubble Distribution in Direct Formic Acid Fuel Cells. *Journal of The Electrochemical Society*, 167(13):134502, sep 2020.

[14] Benjamin A. Rizkin, Filip G. Popovic, and Ryan L. Hartman. Review Article: Spectroscopic microreactors for heterogeneous catalysis. *Journal of Vacuum Science and Technology A*, 37(5):050801, sep 2019.

[15] Henrik Bruus. *Theoretical microfluidics*. Oxford university press, 2008.

[16] Martin Z. Bazant, Kevin T. Chu, and B. J. Bayly. Current-Voltage Relations for Electrochemical Thin Films. *SIAM Journal on Applied Mathematics*, 65(5):1463–1484, jan 2005.